



N-enriched porous carbon encapsulated bimetallic phosphides with hierarchical structure derived from controlled electrodepositing multilayer ZIFs for electrochemical overall water splitting

Lijun Yang, Lei Zhang*

College of Chemistry, Liaoning University, 66 Chongshan Middle Road, Shenyang, Liaoning, 110036, People's Republic of China

ARTICLE INFO

Keywords:

Controlled electrodeposition
Multilayer ZIFs
Bimetallic phosphides
N-doped porous carbon
Overall water splitting

ABSTRACT

Cost-effective transition metal-carbon-based hybrids have been widely dedicated to water splitting. Herein, a new three dimensional N-enriched holey carbon layers encapsulated bimetallic phosphides (CoNiP@CN) was synthesized by *in situ* growth, pyrolysis and phosphorization of CoNi mixed zeolite imidazole frameworks (ZIFs) @ZIF-8 films on Ni foam. CoNiP@CN/NF exhibited smaller overpotentials, lower charge transfer resistance and considerable stability for electrocatalysis. The better performance was attributed to the high conductivity of bimetallic phosphides and N-doped porous carbon, the maximum utilization of active sites on 3D conductive substrate and the protection of bimetallic phosphides by N-doped carbon layers. As an integrated high-performance non-noble electrocatalyst for overall water splitting, the CoNiP@CN/NF requires only 1.59 V@ 30 mA cm⁻² in alkaline solution, which is comparable to many other non-noble metal catalysts. This work highlights the construction highly efficient transition metal-carbon-based electrocatalyst derived from well-defined ZIF precursor, promoting the development of low-cost non-noble metal hybrids in energy chemistry.

1. Introduction

Seeking renewable and sustainable energy sources attracts much attention recently due to accelerated consumption of traditional energy sources and aggravation of environmental pollution. Electrochemical splitting of water is one promising way for providing sustainable clean energy [1,2], which involves the cathodic hydrogen evolution reaction (HER) and the anodic oxygen evolution reaction (OER). Both the HER and OER are kinetically sluggish, and require efficient electrocatalysts to lower the large energy barriers for undergoing multistep proton-coupled electron processes [3]. Yet, the single function (benchmark catalysts of Pt for HER, and precious metal or metal oxides for OER, like RuO₂ [4]), reserve scarcity and high cost hamper their large-scale practical utilization in electrolyzes [5,6]. Therefore, developing highly active, cost-effective and stable nonprecious metal bifunctional electrocatalysts, especially transition metal compounds due to their unique d-orbital characteristics, such as oxides [7,8], sulfides [9,10], carbides [11,12], selenides [13–15], nitrides [16,17], metal alloy [18,19], borides [20], and phosphides [21–23], is the key for reducing cost and enhancing the catalytic efficiency for water splitting. Among these potential materials, transition metal phosphides (TMPs, M = Fe, Co, Ni, Cu, Mo, W) [24–29] have emerged as promising electrocatalysts

because of their metallic nature with high electrical conductivity. However, most of these catalyst preparations are based on nanoparticles that show a high surface area, but also have some disadvantages such as uncontrolled agglomeration, higher series resistances, still-existing templates, and easier oxidation, the conductivity changes along with the crystal structure and stoichiometric form. And most of these electrocatalysts are in the powder form and need to be mixed with a binder such as Nafion solution in order to paste on the conductive substrate. A large portion of the catalyst surface is thus blocked as “inert surface,” which will not participate in electrochemical reactions. Meanwhile, experimental and theoretical investigations have revealed that introduction of more electronegative P atoms into transition metals greatly restricts electron delocalization in the metals, resulting in lower conductivity [30,31].

Therefore, further improvements are needed in their conductivity and stability to ensure performance comparable to that of noble metals. The efficient method to improving the catalysts including three ways: firstly, doping of heteroatoms in phosphides with different atoms to enhance the metallic character and hence improve their intrinsic conductivity, undoubtedly metal-rich phosphides exhibited higher catalytic activity than corresponding monometallic phosphides; secondly, combining the metal phosphides with conducting substrates (such as Ni

* Corresponding author.

E-mail address: zhanglei63@126.com (L. Zhang).

<https://doi.org/10.1016/j.apcatb.2019.118053>

Received 4 June 2019; Received in revised form 30 July 2019; Accepted 3 August 2019

Available online 09 August 2019

0926-3373/ © 2019 Elsevier B.V. All rights reserved.

foam(NF), carbon cloth, et.al.) can not only improve electronic conductivity, but also expose more active sites and inhibit catalysts agglomeration; third, binder-free electrode increases the conductivity and improves the utilization rate of TMPs as compared to the traditional binder-containing pasted electrode. Meanwhile, water splitting (HER and OER) in alkaline medium can simplify the water electrolyzer system by simply immerse an anode and a cathode in a single container containing alkaline electrolyte [32–35], avoiding the disadvantage of electrocatalysts in acid medium like expensive, scarce, acid insoluble, and unstable. Therefore, significant efforts have been made to achieve high efficient overall water splitting in alkaline medium by tailoring the chemical state and morphological features of the earth-abundant bifunctional electrocatalysts [35].

Considering that zeolitic imidazolate frameworks (ZIFs) can be effectively transformed into the hybridization with nitrogen-doped porous carbon materials and high metal ion contents through directly pyrolyzed, which are expected to be good candidates as the precursor template to design various porous nanostructured metal-carbon hybrid materials [36] and the corresponding phosphide derivatives. Herein, a highly active and stable bifunctional water-splitting N-doped holey carbon layers encapsulated bimetallic phosphides (CoNiP@CN) electrocatalyst was synthesized through *in situ* growth, pyrolysis and phosphorization ZIFs on highly porous and conductive nickel foam (Scheme 1). The hierarchical CoNiP@CN is innovatively optimized by selective doping highly active nitrogen. The superior performance with robust durability is mainly attributed to bimetallic phosphides and collaborative advantages of N-doped holey carbon layers, as well as the 3D porous conductive substrate. The synergetic effect of this uniquely configured electrocatalyst exhibits outstanding HER and OER activities in alkaline media, which requires a cell voltage as low as 1.59 V to achieve a water splitting current density of 30 mA cm⁻² in alkaline solution with robust durability, thus compare favourably with the Co-Ni-P based bifunctional electrocatalysts reported so far. This work provides a new insight into the design of novel non-noble metal bifunctional catalysts for highly efficient overall water splitting.

2. Experimental section

2.1. Chemicals and reagents

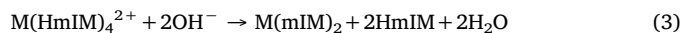
2-methyl-imidazole (C₄H₆N₂, 99%) was supplied by Aladdin Co. Ltd (Shanghai). Cobalt nitrate hexahydrate (Co(NO₃)₂·6H₂O, 98%), nickel nitrate hexahydrate (Ni(NO₃)₂·6H₂O, 98%), zinc nitrate hexahydrate (Zn(NO₃)₂·6H₂O, 98%), sodium hypophosphite (NaH₂PO₂, 98%), potassium hydroxide (KOH, 85%), methyl alcohol (CH₃OH). All other chemicals were of analytical reagent grade and bought from Sinopharm chemical reagent Co. Ltd (Shenyang).

2.2. Electrosynthesis of mixed CoNi ZIFs @ZIF-8 films

The Ni foams (10 × 20 × 1 mm) were pretreated with diluted

hydrochloric acid (3 M), ethanol and deionized water, each for 15 min, to clean the surface. The electrosynthesis of precursor films was operated in an electrochemical cell in a three-electrode configuration with as prepared materials as working electrode, Pt wire as the counter electrode, and saturated calomel electrode (SCE) as reference electrode. The synthesis of mixed CoNi ZIFs@ZIF-8 films process included two steps(Scheme 1): firstly, the electrolyte for the electrosynthesis of mixed CoNi ZIFs was prepared by adding 2.5 mM of Co(NO₃)₂·6H₂O, 2.5 mM of Ni(NO₃)₂·6H₂O and 0.02 M of 2-methylimidazole (HmIM) into 50 mL 95% methanol (with 5% H₂O); a constant voltage of -5.0 V vs. SCE was carried out for precursor films growth with electrosynthesis time of 300 s; secondly, the electrolyte for the electrosynthesis of ZIF-8 was prepared by adding 5 mM of Zn(NO₃)₂·6H₂O and 0.02 M of 2-methylimidazole (HmIM) into 50 mL 95% methanol (with 5% H₂O), and a constant voltage of -5.0 V vs. SCE was carried out for precursor films growth with electrosynthesis time of 400 s. The mixed CoNi ZIFs and ZIF-8 film were prepared via the similar method for comparisons.

Once the metal ions and HmIM mixed, M(HmIM)₄²⁺ (M = Co and Ni) is rapidly generated (Eq. (1)) [37]. In the following subsequent electrochemical synthesis process, OH⁻ is formed by reducing H₂O on the working electrode (Eq. (2)), and then the resulting OH⁻ is further reacted with M(HmIM)₄²⁺ to form M(mIM)₂ (Eq. (3)) and deposited on the surface of substrate [38].

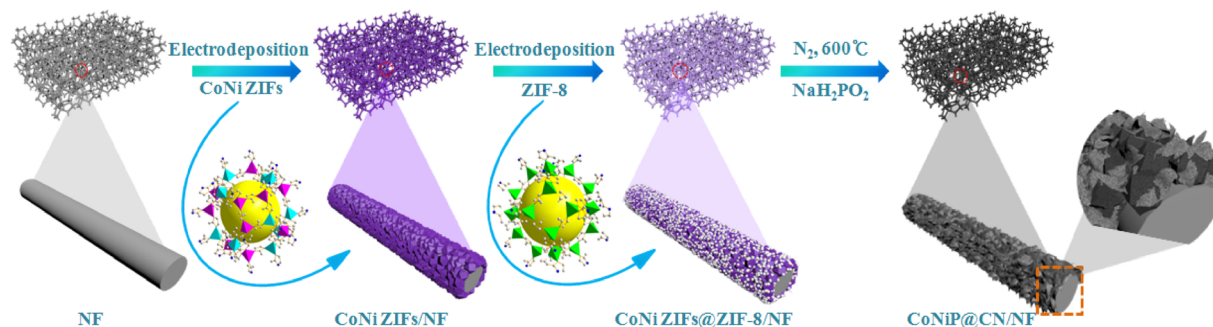


2.3. Preparation of CoNiP@CN films

The as-prepared precursor film was placed at the middle of a porcelain boat and 2.0 g of NaH₂PO₂ was placed at the upstream side. The porcelain boat was put in a tube furnace and directly pyrolyzed at 600 °C (heating rate: 2 °C min⁻¹) in N₂ atmosphere for 2 h to yield CoNiP@CN/NF. The mass loading of active material of CoNiP@CN composites on NF is estimated to be ≈ 6.3 mg cm⁻².

2.4. Characterization

The morphology and microstructures of the as-prepared materials were examined by a scanning electron microscope (SEM, SU8000, Hitachi Co., Japan) operated at 10.0 kV. Transmission electron microscopy (TEM) was performed on a transmission electron microscopy (TEM, 2100 F, JEOL Co., Japan) with an accelerating voltage of 200 KV. Powder X-ray diffraction (XRD) patterns were collected on Diffractometer (XRD, D5000, Siemens Co., Germany), using Cu-Kα radiation (λ = 0.1542 nm) in the 2θ range of 10 - 80 with a scanning rate of 1° min⁻¹. The chemical state was analysed by X-ray photoelectron spectroscopy (XPS) analysis performed on a Thermo Electron Corporation ESCALAB 250 Xi and the binding energies were calibrated



Scheme 1. Illustration for the synthesis of CoNiP@CN composite.

using the C 1s peak at 284.5 eV. Raman spectra were collected using a Micro-Raman spectrometer system (Renishaw inVia system equipped with an integral microscope(Leica)) using 532 nm. Deionized water used throughout experiments was purified using a Sartorius Arium 611 system (Sartorius, Göttingen, Germany).

Both hydrogen evolution reaction (HER) and oxygen evolution reaction (OER) testing were performed in a standard three-electrode system using an electrochemical work station (CHI 660D, Shanghai ChenHua Instruments Co., China). A platinum wire and SCE electrode were used as the counter and reference electrodes, respectively. In 1.0 M KOH, the potentials used in this work with respect to the SCE electrode was converted to the potential versus the reversible hydrogen electrode (RHE) according to $E_{\text{RHE}} = E_{\text{SCE}} + 0.242 + 0.059\text{pH}$.

To prepare Pt/C and IrO₂ catalytic electrodes, 10 mg 20% Pt/C or IrO₂ and 20 μL 5 wt% Nafion solution were dispersed in 1 mL water/ethanol solvent (250 mL ultrapure water and 750 mL ethanol). The mixed solution was then ultrasonically treated for 60 min to form a homogeneously distributed catalyst ink. A suitable amount of the catalyst ink was uniformly drop-cast onto the Ni foam and left to dry in air.

Before each HER experiment, the working electrode was continuously cycled at least 60 times between 0 and -0.4 V vs. RHE at a scan rate of 100 mV s⁻¹ in N₂-saturated electrolyte until a stable cyclic currents indicating a stable solid/liquid interface. Linear scan voltammograms (LSVs) were collected at a scan rate of 5 mV s⁻¹ from 0 and -0.4 V vs. RHE for HER corrected by 97% IR-correction. The electrochemical double layer capacitance (*C_{dl}*) was investigated by cyclic voltammograms in a narrow potential range from 0.1 to 0.25 V vs. RHE. ΔJ was measured at 0.2 V vs. RHE and plotted against the scan rate, then the resulting linear slope of the plot was twice the *C_{dl}* value.

Before each OER experiment, the working electrode was continuously cycled at least 60 times between 1.15 and 1.8 V vs. RHE at a scan rate of 100 mV s⁻¹ before collecting OER data. Linear scan voltammograms (LSVs) were collected at a scan rate of 5 mV s⁻¹ from 1.15 and 1.8 V vs. RHE for OER corrected by 97% IR-correction. The electrochemical double layer capacitance (*C_{dl}*) was investigated by cyclic voltammograms in a narrow potential range from 1.05 to 1.15 V vs. RHE. ΔJ was measured at 1.09 V vs. RHE and plotted against the scan rate, then the resulting linear slope of the plot was twice the *C_{dl}* value.

Electrochemical impedance spectrum (EIS) was collected by applying an AC voltage with 5 mV amplitude in a frequency range from 100,000 to 1 Hz and recorded at a voltage of -0.22 V vs. SCE. For overall water splitting (both HER and OER) tests, the CoNiP@CN grown on Ni foams were employed as both anode and cathode. To remove the gas bubble during electrocatalysis process, a rotation rate of 1600 rpm was applied for OER and HER measurements. In terms of measuring the electrochemical performances, the chronopotentiometric measurement was performed at a current density of 10 mA cm⁻² and 30 mA cm⁻² for HER and OER on CoNiP@CN/NFs, respectively.

3. Results and discussion

The CoNiP@CN films were prepared through a two-step electrodeposition mixed-metal ZIFs@ZIF-8 approach following pyrolysis and phosphorization. The morphologies of the as-prepared electrodes were examined by scanning electron microscopy (SEM), and the corresponding results were displayed below. As shown in Fig. 1a, the surface of the pristine acid-treated Ni foam had a three-dimensional (3D) structure with a rough surface with the coverage of the polygonal platelets. Firstly, direct electrodeposition of CoNi ZIFs in the presence of Ni foam generated the mixed metal ZIFs-based/NF precursor. As shown in the inset of Fig. 1b, the precursor film was purple colored and uniformly grown over the entire surface of the skeleton after an electrosynthesis time of 300 s. The surface was obviously distinct from Ni foam, on which the deposits were tightly packed with many polyhedrons with an average size of ~200 nm. After pyrolysis and phosphorization, the surface ZIFs film was in situ converted into a

hierarchical structure of phosphide and carbon hybrids. It could be seen from Fig. 1c, the skeleton was rougher than precursor film (inset in Fig. 1c), and the dense and uniform polyhedrons grew to fuse together to form uneven multiple ranges of wrinkles while the external composites began to grow vertically with the continuous blowing nitrogen.

After the second step of electrodeposition time of 400 s, white colored ZIF-8 film was uniformly coated on the surface of mixed metal ZIFs film, and the Ni framework broaden obviously (inset in Fig. 1d). The surface was covered with amounts of small nanoparticles (29.8 ± 0.4 nm) and still there were many exposed polyhedrons corresponding to the mixed CoNi ZIFs shown in Fig. 1d, which guaranteed the appropriate active sites for electro-catalysis. The 3D hierarchical CoNiP@CN was achieved via in situ pyrolysis and phosphorization of the mixed metal ZIFs@ZIF-8 films. Compared to CoNiP/NF, the surface of Ni skeleton became much rougher and wider with many vertically-grown sheets (Fig. 1e). During the calcination process at high temperature, superficial Zn was evaporated leaving many pores and with the increase of organic ligands, the external composites transformed into larger surface area and thinner vertically-grown sheets with continuous inert gas flow (Fig. 1f). This unique hierarchical architecture with abundant nanosheets and porous structure not only offers minimum diffusive resistance to mass transport on a large electrode/electrolytes interface for charge-transfer reaction [39], but also inhibited metal-based particles stacking and aggregation, which were important in the later electrocatalytic processes.

Transmission electron microscopy (TEM) image of CoNiP@CN exfoliated off from the electrode by ultrasonic were shown in Fig. 2. It was revealed that clearly visible nanoholes existed in the nanosheets (Fig. 2a), which were made up of amounts of homodisperse nanoparticles. The porous channels provided the pathways for electron conduction and thus promoted the electron transfer and accelerated the bubble (H₂ and O₂) diffusion on the surface of the electrode. Some randomly stacked carbon layers indicating more defects and edges were also present in the CoNiP@CN (marked by blue circles) (Fig. 2b) [40]. Particularly, abundant small dark domains about 5–8 nm were observed to be encapsulated within the carbon matrix (marked by red circles). As depicted in Fig. 2c, the high-resolution transmission electron microscopy (HRTEM) image showed the clear lattice fringes of 0.22 nm, 0.19 nm and 0.17 nm could be readily indexed to the (111), (210) and (300) facets of the hexagonal CoNiP, respectively [34,41]. Meanwhile, it should be noted that the warped graphitic layers (Fig. 2d) should promote the exposure of abundant edges on the carbon surface, which have been proved to be beneficial for the enhanced electrocatalytic properties [38,42].

The crystal-phase structure of the as-prepared samples were analyzed by XRD. As shown in Fig. 3a, a typical peak centered at 26.5°, attributed to the (002) facet of graphitic carbon (PDF card, No.41-1487), and the other peaks located at 41.0°, 44.9°, 47.6°, 54.4°, 54.7° and 55.3° were assigned to the (111), (201), (210), (002), (300) and (211) planes of CoNiP with pure hexagonal phase (PDF card, No.71-2336), respectively, which is consistent with the TEM results. The diffraction peaks at about 22.5° and 28° might correspond to CoP₃ or NiP₃, indicating that there was a little CoP₃ or NiP₃ generated during phosphating process. Moreover, Raman spectroscopy analysis revealed that there were two characteristic peaks located at 1330 cm⁻¹ (D band) and 1580 cm⁻¹ (G band), corresponding to disordered and graphitized carbon, respectively. The measured D band to G band intensity ratio (*I_D*/*I_G*) from CoNiP@CN (0.81) is lower than that of CoNiP (0.87), suggesting a higher degree of graphitization in CoNiP@CN (Fig. 3b).

X-ray photoelectron spectroscopy (XPS) tests were further conducted to confirm the composition of CoNiP and CoNiP@CN holey nanosheets composites. As shown in Fig. 4a, XPS survey spectrum confirmed the chemical composition of CoNiP@CN included Zn, Ni, Co, P, C, N, and O elements. Residual Zn could attribute to the relative low pyrolysis temperature, and Zn spectrum in XPS has shown in Fig. S1: the two peaks located at 1045.1 and 1022.0 eV in high-resolution Zn 2p

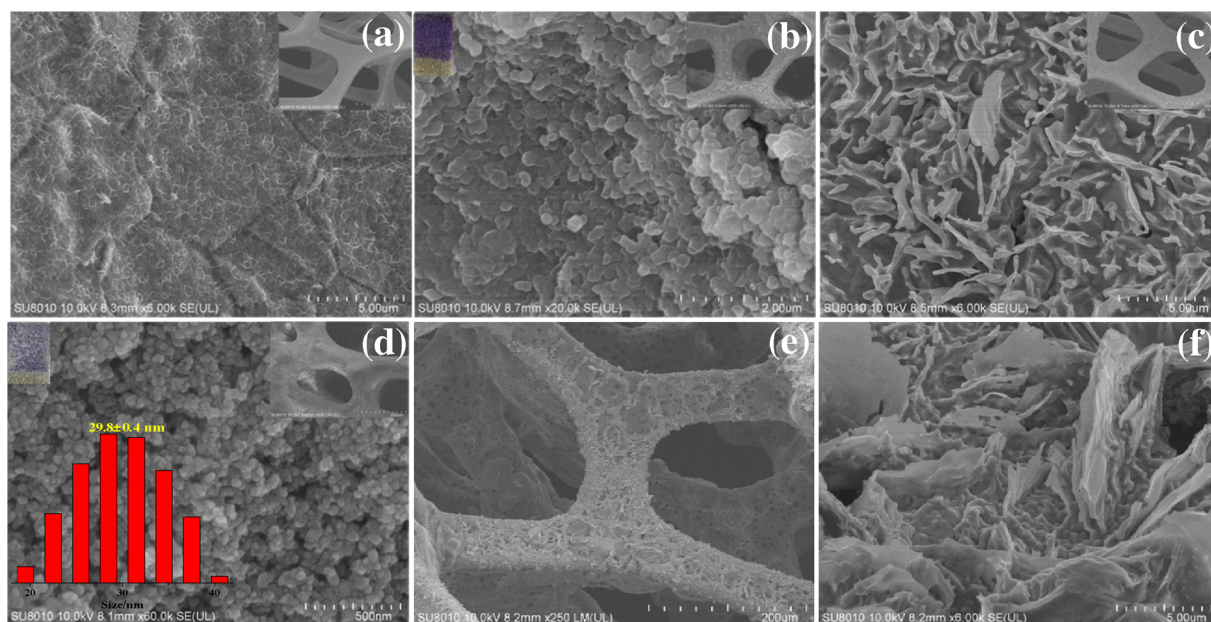


Fig. 1. SEM images of Ni foam(a); CoNi ZIFs/NF(b); CoNiP/NF(c); CoNi ZIFs@ZIF-8/NF (d); CoNiP@CN/NF(e, f).

spectrum corresponds to Zn 2p_{1/2} and Zn 2p_{3/2}, respectively. The high-resolution Co 2p XPS spectrum of CoNiP catalyst revealed that the binding energy (B.E.) of the Co 2p_{3/2} peaks (Fig. 4b) located at 779.6, 781.9 and 785.4 eV [43], which could be assigned to the Co-P, Co-N and satellite peak, respectively. The Co 2p_{1/2} peaks of CoNiP catalyst have similar peak assignment with Co 2p_{3/2} [44]. The Ni 2p core level spectrum (Fig. 4c) also can be fitted into three pairs of peaks which are attributed to the Ni-P (872.1 eV and 854.7 eV), Ni-N (874.3 eV and 856.6 eV) [45,46] and the satellite feature (879.5 eV and 861.5 eV) [47,48]. And in the P 2p region of CoNiP (Fig. 4d), the B.E. of the P 2p peaks located at 129.7 (P 2p_{3/2}) and 130.4 (P 2p_{1/2}) can assigned to P bonded to Ni or Co [49,50]. The peak at higher B.E. (~134.2 eV)

associated the oxidized P species comes from the oxidation in contact with the air [51]. Compared to metallic Ni (852.6 eV), Co (778.3 eV), and P (130.1 eV), Ni and Co 2p 2p_{3/2} are positively shifted and P 2p is negatively shifted, which are mainly due to the partial electron transfer from metal to P. However, in CoNiP@CN the binding energies of P 2p_{3/2} (129.2 eV), P 2p_{1/2} (129.8 eV) and P-O (133.5 eV) further negative shifted obviously, indicating the electron-rich P sites, which are proton-acceptor sites, can decrease the energy barrier to proton binding [52]. The electronic structure modulation of CoNiP@CN was beneficial to the adsorption and desorption process between reactant and resultant molecules [53]. Additionally, the intensity of peak P-O obviously decreased, indicating that carbon layers could decrease the phosphides be

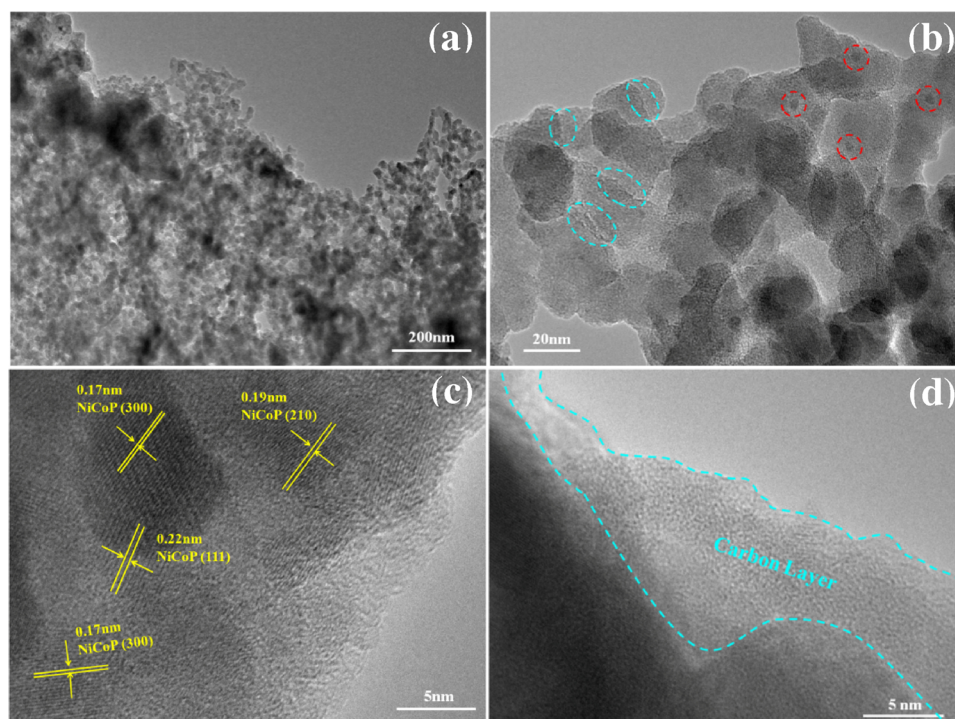


Fig. 2. TEM images(a, b) and HRTEM images(c, d) of CoNiP@CN.

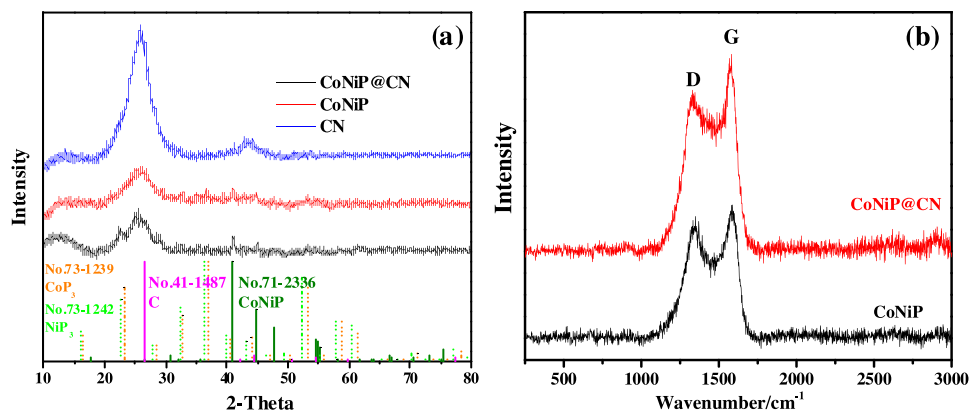


Fig. 3. (a) XRD of CoNiP@CN, CoNiP and CN; (b) Raman spectra of CoNiP and CoNiP@CN.

oxidized by air.

The high-resolution XPS spectrum of C 1s with a tail lying in the higher binding energy can be fitted into two bands (Fig. 4e): the strong intense peak at 284.5 eV belongs to the combination of the sp^2 C=C and sp^3 C-C [54], while the presence of C-N bonds at 285.3 eV indicates that N atoms have been doped into the graphitic domains, which would generate more active sites and enhance electrical conductivity [48,55]. Meanwhile, N dopants could activate adjacent C atoms to enhance reactants or intermediates adsorption in CoNiP@CN. To clarify the forms of existing N species, N 1s spectra were further analyzed (Fig. 4f). The results showed that nitrogen mainly existed in the form of pyridinic-N (398.2 eV), Metal-N_x (399.1 eV), pyrrolic-N (400.2 eV) and graphitic-N (401.3 eV), respectively [56]. The presence of Metal-N_x bonding structure provides evidence of the interaction between metal and heteroatom doped graphitic carbon supports. It was generally accepted that pyridinic-N, pyrrolic-N and graphitic N play significant roles in the HER and OER processes [57,58] are dominated in CoNiP@CN. The existence of pyrrolic-N and pyridinic-N species in

Table 1

N 1s XPS elemental analysis of CoNiP and CoNiP@CN samples.

Samples	Total N (At%)	pyridinic-N (%)	pyrrolic-N (%)	Metal-N _x (%)	graphitic-N (%)
CoNiP	7.14	45.15	21.42	14.76	18.67
CoNiP@CN	10.21	46.38	23.48	16.65	13.50

catalyst could improve the electrocatalytic activity by interacting with H^+ for HER [57] or bind to OER intermediates (such as O^* , OOH^* , or OH^*) with a appropriate force [59]. Among these N constituents shown in Table 1, the largest percentage of pyridinic-N can effectively absorb the oxygen molecules, because the carbon near the pyridinic-N sites provides the main Lewis basic sites [60,61]. The higher N dopants can not only serves as a robust support for effectively protecting the metal centers from aggregation, but also modulate the electronic structure of CoNiP via the interplay between heteroatom doped carbon and metal phosphides. Overall, all of results above confirmed that the successful

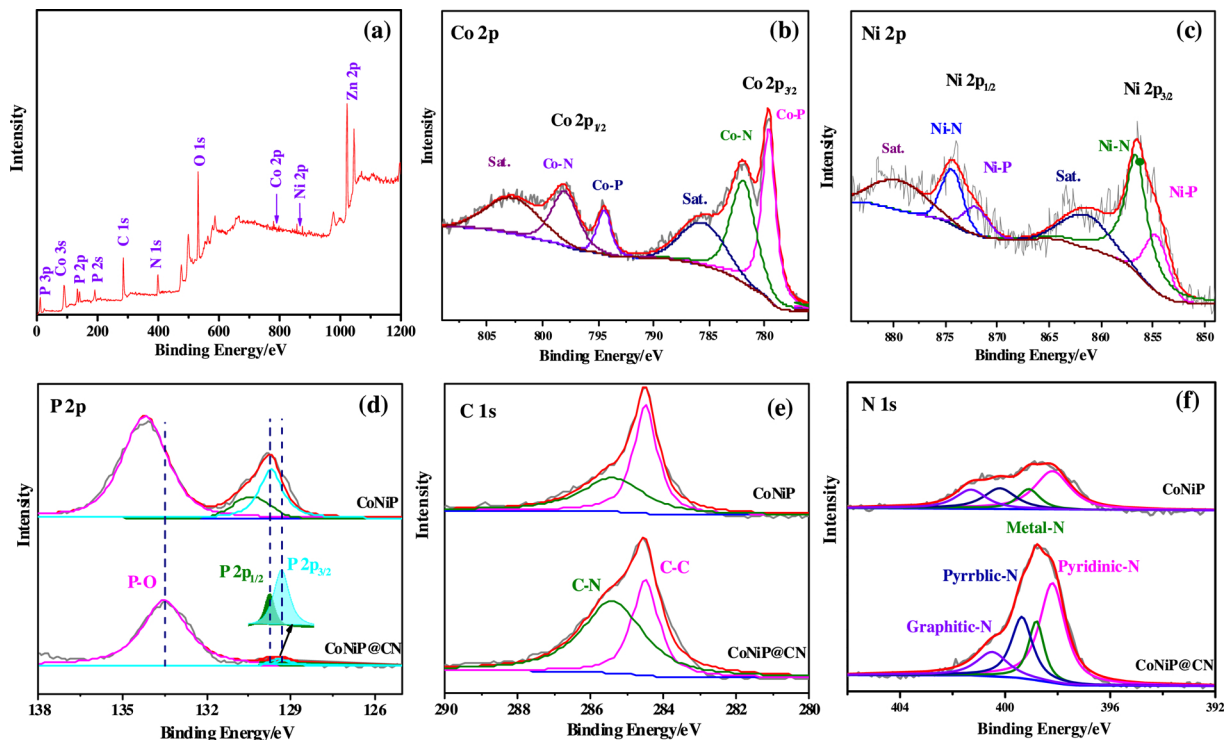


Fig. 4. (a) XPS survey spectrum; high-resolution XPS spectra: (b) Co 2p; (c) Ni 2p of CoNiP@CN; (d) C 1s; (e) N 1s and (e) P 2p of CoNiP and of CoNiP@CN, respectively.

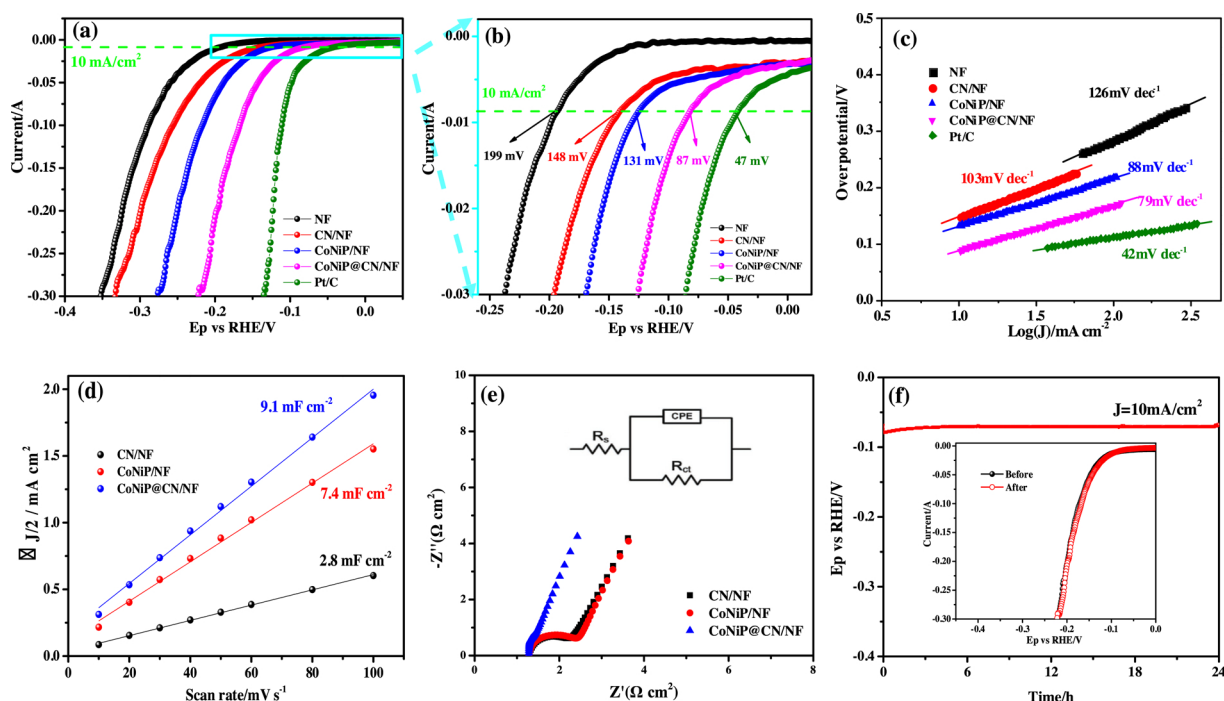


Fig. 5. (a, b) Polarization curves and their enlarged views; (c) the corresponding Tafel plots; (d) the current density versus scan rate of the NF, CN/NF, CoNiP/NF, CoNiP@CN/NF and Pt/C; (e) Nyquist plots of CN/NF, CoNiP/NF and CoNiP@CN/NF; (f) Chronopotentiometry (V-t) curve of CoNiP@CN/NF during HER at a constant current density of 10 mA cm^{-2} in 1.0 M KOH (inset: LSV curves before and after durable test).

obtainment of N-doped holey carbon layers encapsulated bimetallic phosphides (CoNiP@CN) and both CoNiP species and nitrogen doping carbon would be beneficial for HER and OER.

Based on the above understanding, the performance of CoNiP@CN and control materials (NF, CN and CoNiP) for water splitting was studied extensively. Firstly, the electrocatalytic activities of the as-synthesized samples were investigated as electrocatalysts for HER on a three-electrode configuration in 1.0 M KOH electrolyte. The polarization curves with IR correction were shown in Fig. 5a-b. Compared with NF, CN and CoNiP, the CoNiP@CN electrode exhibits significantly improved HER catalytic properties, displaying a low overpotential of 87 mV and 198 mV to achieve a current density of 10 mA cm^{-2} and 200 mA cm^{-2} , indicating a highly efficient cathode for generating hydrogen from water. The corresponding Tafel slopes of CoNiP@CN catalyst (79 mV dec^{-1}) were also smaller than that of CoNiP (88 mV dec^{-1}), CN (103 mV dec^{-1}) and NF (126 mV dec^{-1}) in 1.0 M KOH , respectively (Fig. 5c), revealing more favorable electrocatalytic kinetics on CoNiP@CN catalyst for HER. The value of Tafel slope of CoNiP@CN catalyst also indicated that the HER process undergo a Volmer-Heyrovsky pathway [62]. This appreciable HER catalytic activity can be attributed to the structural features of CoNiP@CN, where the CoNiP nanoparticles engaged in ultrathin N-doped holey carbon enable the high electro-negative P atom can attract electron from metal atom and become a negatively charged center (σ^-), which can act as absorption sites for positively charged H protons while metal centers (σ^+) act as a hydride acceptor [63]. Additionally, the unique hierarchical holey structure has a higher wettability, which could enhance the electrolyte penetration and augment the contact degree between reactants and active sites, and thus facilitate the HER kinetics. Meanwhile, the HER performance is superior to monometallic phosphides ($\text{Ni}_2\text{P@CN}$ and CoP@CN , shown in Fig. S2).

To better understand the intrinsic electrocatalytic activity of CoNiP@CN, the electrochemical surface areas (ECSAs) was investigated by measuring the double-layer capacitance (C_{dl}) at the liquid-solid interface. As shown in Fig. S3a-c, we performed cyclic voltammograms (CVs) curves at different scan rates in a non-Faradaic region (0.1 to

0.25 V vs RHE). The capacitive currents of all the catalysts were collected at the same potential of 0.2 V vs RHE, and the plot was shown in Fig. 5d. As we expected, the estimation C_{dl} of CoNiP@CN (9.1 mF cm^{-2}) getting from the slope of the fitting line is much higher than those of CN (2.8 mF cm^{-2}) and CoNiP (7.4 mF cm^{-2}), suggesting that it exhibits a higher electrocatalytic activity probably due to the larger electrochemical surface area and higher surface roughness [64]. Therefore, we attributed the great ECSA to the unique and robust hierarchical porous architecture generated abundant interfaces, exposed more catalytically active sites and facilitated charge/mass transport during the electrocatalytic processes, resulting in the remarkable proliferation of electrocatalysis for the HER.

To investigate the catalytic kinetics and interfacial properties under HER process, the electrochemical impedance spectroscopy (EIS) measurements were carried out (Fig. 5e). The semicircles in the high-frequency and low-frequency range of the Nyquist plot attributed to the charge-transfer resistance R_{ct} and solution resistance R_s , respectively, are related to the electrocatalytic kinetics and a lower value corresponds to a faster reaction rate [65]. The Nyquist plots indicate that CoNiP@CN catalyst showed a smaller semicircle diameter ($R_{ct} \approx 0.2 \Omega$) than that of CN ($R_{ct} \approx 1.8 \Omega$) and CoNiP ($R_{ct} \approx 2.2 \Omega$) catalyst, suggesting a favorable charge transport in the electrode interior owing to the vectorial electron transport in CoNiP@CN network and the excellent electrical connection between CoNiP@CN and conductive Ni foam substrates.

As another important criterion to evaluate the activity of electrocatalyst, the durability of CoNiP@CN was consecutively conducted at 10 mA cm^{-2} . As shown in Fig. 5f, the CoNiP@CN/NF showed impressive stability after testing for 24 h , which was also supported by the nearly overlap of LSV curves before and after durable test (inset in Fig. 5f). The high durability of CoNiP@CN may be caused by the good protection of CoNiP nanoparticles embedded in the N-doped porous carbon. As illustrated above, the pores in CoNiP@CN can expose many catalytic active sites for HER. Furthermore, the N-doped porous carbon were found to act as a bridge, which improved the mechanical performance of CoNiP nanoparticles, and also promoted the rapid charge-

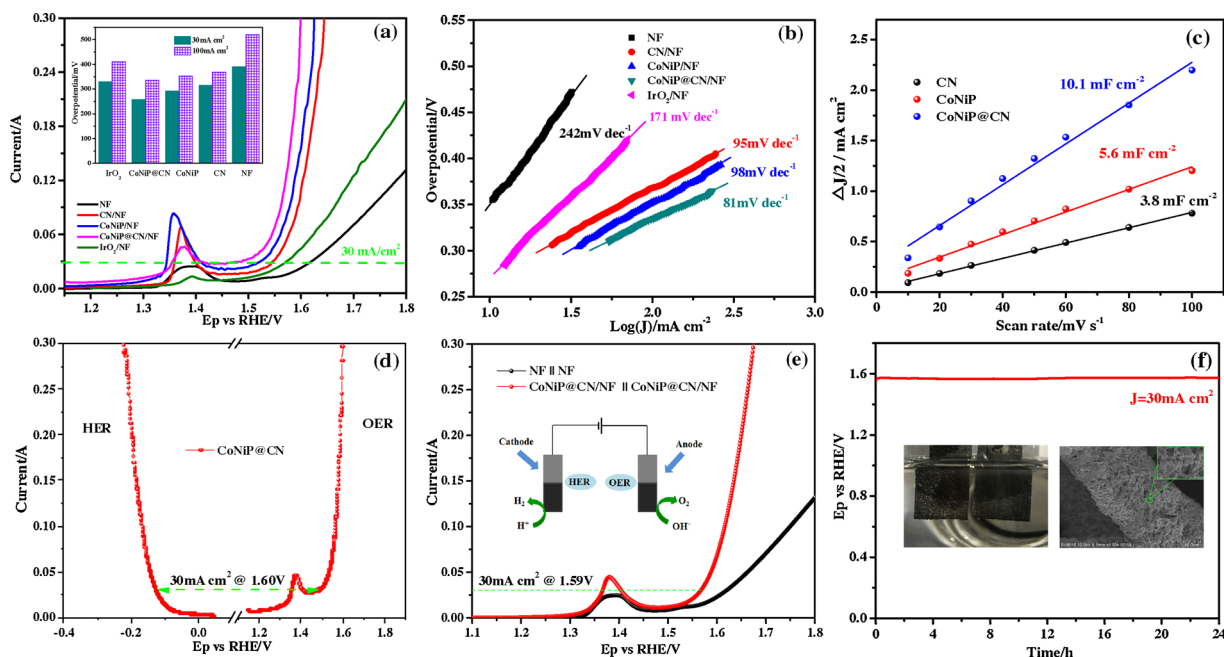


Fig. 6. (a) Polarization curves (inset: their overpotential at 30.0 mA cm⁻²); (b) the corresponding Tafel plots of NF, CN/NF, CoNiP/NF, CoNiP@CN/NF, and IrO₂/NF; (c) the current density versus scan rate of CN/NF, CoNiP/NF and CoNiP@CN/NF; (d) Polarization curves of CoNiP@CN/NF for HER and OER. (e) Polarization curves of the CoNiP@CN/NF || CoNiP@CN/NF electrode and pure Ni foam || Ni foam in 1.0 M KOH solution without IR compensation in a two-electrode system; (f) Chronopotentiometric (V-t) curve of overall water splitting at a constant current density of 30 mA cm⁻². (Inset-left: Photograph of the electrode surface when overall water splitting at 30 mA cm⁻²; Right: SEM images of CoNiP@CN/NF after 24 h electrolysis process.).

transfer reaction, resulting in prolonged durability. Thus, these advantages resulting from the in-situ grown 3D network holey structure on Ni foam, such as large specific surface area, more active sites, efficient charge transfer, and favorable mass transport, conjointly contribute to the excellent HER activities of CoNiP@CN/NF.

Besides excellent HER performance, the CoNiP@CN can especially perform very high catalytic activity of OER for electrochemical oxidation of water to produce oxygen at the same time. The OER catalytic performance of the CoNiP@CN catalyst was then assessed in 1.0 M KOH solution. CoNiP/NF and CN/NF were also tested for comparison. Fig. 6a showed their linear sweeps voltammograms in an anodic direction (IR corrected) with a scan rate of 5 mV s⁻¹, an obvious anodic peak around 1.40 V (versus RHE) assigned to the Ni²⁺/Ni³⁺ redox reaction can be clearly observed in the LSV profiles of all samples [66]. The CoNiP@CN catalyst exhibits the highest electrocatalytic activity with the lowest overpotential of 258 mV to achieve the current density of 30 mA cm⁻² compared with CoNiP (293 mV), CN (316 mV), NF (390 mV), and IrO₂ (356 mV) respectively, further indicating the superior catalytic behavior for OER of CoNiP@CN catalyst. Meanwhile, the oxide peak of Ni in CoNiP@CN/NF was obviously lower than those of the other two electrodes, further confirming the protection of the N-doped holey carbon layers. The corresponding Tafel curves (Fig. 6b) of these catalysts also show the smallest Tafel value (81 mV dec⁻¹) of CoNiP@CN compared with CoNiP (95 mV dec⁻¹), CN (98 mV dec⁻¹), NF (242 mV dec⁻¹) and IrO₂ (171 mV dec⁻¹) suggesting higher OER rates of CoNiP@CN catalyst. Meanwhile, the OER performance is superior to monometallic phosphides (Ni₂P@CN and CoP@CN, shown in Fig. S2). The amounts of catalytically active sites on the as-prepared electrodes were roughly estimated from *Cdl* by measuring CV curves at different scan rates in a non-Faradaic region (1.05 to 1.15 V vsRHE) (shown in Fig. S4a-c). The determined *Cdl* for CoNiP@CN is much higher than that of CoNiP and CN in Fig. 6c, indicating a larger active surface area and more exposed active sites, which would contribute to enhanced OER performance. The durability of CoNiP@CN was consecutively conducted at 30 mA cm⁻² as shown in Fig. S5, the CoNiP@CN/NF showed impressive stability after testing for 24 h, which was also supported by the nearly

overlap of LSV curves before and after durable test (inset in Fig. S5). Experimental results (Fig. S6) have shown that CoNiP@CN has changed to CoNiP₄O₁₂@CN during electro-oxidation scan in the OER process. The as-prepared phosphides were able to facilitate the in situ formation of phosphates, improve the redox activity of the catalyst surface as a result of lowering activation energy of oxygen adsorption, thus show good electrocatalytic activity [32,67].

The above results indicate that CoNiP@CN catalyst can serve as a bifunctional electrocatalyst for overall water splitting with superior activity and stability. Therefore, we evaluated its overall water splitting activity in 1.0 M KOH using two electrode configuration using CoNiP@CN catalyst as both a cathode for HER and an anode for OER. The polarization curves (Fig. 6d) showed that the overall potential window between HER and OER for the CoNiP@CN/NF could be 1.60 V at 30 mA cm⁻². The voltage difference was consistent with the cell voltage of 1.59 V (Fig. 6e) at the same current density tested in the overall water-splitting system. Large numbers of bubbles were produced from both cathode (H₂) and anode (O₂) during electrolysis. The overall water splitting performance of CoNiP@CN catalyst is equal to or better than most of reported nonprecious metal phosphides electrocatalysts (Table S1). The water electrolyzer durability was examined at the current density of 30 mA cm⁻² (Fig. 6f). The electrolysis process could be sustained for at least 24 h, revealing the outstanding stability of the CoNiP@CN catalyst for overall water splitting. The relevant SEM images of CoNiP@CN/NF after 24 h electrolysis process certify that the morphology was hardly altered.

The superior catalytic performance of hierarchical CoNiP@CN/NF in overall water splitting is ascribed to several factors: (i) Bimetallic phosphide can not only enhance the metallic character and hence improve their intrinsic conductivity, offer a favorable surface electronic structure and coordination nature that enable the enhanced catalytic reactivities, but also induce the change of active sites and enable thermodynamically more efficient hydrogen/oxygen adsorption process on the catalyst surface. Meanwhile, the electrons diffusion from metal to P in CoNiP@CN is expected to increase the electron transfer and decrease the energy barrier for the adsorption-desorption process of

reactant, thus improving the related electrocatalytic activity. (ii) The introduction of heterogeneous atoms can not only regulate the coordination environment of metal atoms in ZIFs, but also provide certain steric hindrance to alleviate the agglomeration phenomenon in the in situ pyrolysis and phosphorization process. (iii) The in situ carbonization of organic ligands around metal sites during pyrolysis always forms N-doped carbon matrix with nanoporous structures, which can enhance the mass transfer during catalytic reactions, facilitate the exposure of active sites, and provide more sites for the adsorption of reactant and intermediate. The in situ formed carbon shell on the surface of electrocatalyst can significantly enhance the durability of the CoNiP@CN. Based on the analysis, a synergistic effect between the active bimetallic phosphides and N-doped porous carbon matrix is believed to be reasonable for improving the performance of the CoNiP@CN. This work highlights the potential application of CoNiP@CN/NF as one of the promising bifunctional catalysts for clean and renewable energy utilization.

4. Conclusions

In summary, we have successfully synthesized a hierarchical films of CoNiP@CN on 3D Ni foam as high-performance bifunctional HER/OER electrocatalyst by in situ pyrolysis and phosphorization of a multilayer ZIF films obtained by a two-step electro-deposition. The rationally designed and synthesized heterometallic phosphides composites CoNiP@CN with controlled morphologies and compositions can efficiently catalyze both HER and OER in alkaline electrolyte. The superior performance with robust durability is mainly attributed to unique bimetallic phosphides and collaborative advantages of N-doped holey carbon layers, as well as the 3D porous conductive substrate, which will enable them to facilitate electron transport, improve charge-transfer characteristics, avoid uncontrolled agglomeration, protect metal phosphides against oxidation, and expose more active sites, the coupled interactions among these components, leading to high electrocatalytic activities and outstanding kinetics for both HER and OER. As an integrated high-performance non-noble electrocatalyst for overall water splitting, which requires a cell voltage as low as 1.59 V to achieve a water splitting current density of 30 mA cm⁻² in alkaline solution with robust durability.

Declaration of Competing Interest

The authors declare that they have no known competing financial interests or personal relationships that could have appeared to influence the work reported in this paper.

Acknowledgements

This project was supported by the National Nature Science Foundation of China (NSFC51672116) and Liaoning Province Science and Technology Planning Project (20180551203). The authors also thank their colleagues and other students who participated in this study.

Appendix A. Supplementary data

Supplementary data associated with this article can be found, in the online version, at <https://doi.org/10.1016/j.apcatb.2019.118053>.

References

- [1] J.A. Turner, *Science* 305 (2004) 972–974.
- [2] X. Du, J. Huang, J. Zhang, Y. Yan, C. Wu, Y. Hu, C. Yan, T. Lei, W. Chen, C. Fan, J. Xiong, *Angew. Chem. Int. Ed.* 58 (2019) 4484–4502.
- [3] J. Yu, Y. Tian, F. Zhou, M. Zhang, R. Chen, Q. Liu, J. Liu, C. Xu, J. Wang, *J. Mater. Chem. A* 6 (2018) 17353–17360.
- [4] Z. Yang, C. Zhao, Y. Qu, H. Zhou, F. Zhou, J. Wang, Y. Wu, Y. Li, *Adv. Mater.* 31 (2019) 1808043.
- [5] Y. Jiao, Y. Zheng, M. Jaroniec, S. Qiao, *Chem. Soc. Rev.* 44 (2015) 2060–2086.
- [6] C.G. Morales-Guio, L.A. Stern, X. Hu, *Chem. Soc. Rev.* 43 (2014) 6555–6569.
- [7] H. Wang, S. Hung, H. Chen, T. Chan, H.M. Chen, B. Liu, *J. Am. Chem. Soc.* 138 (2016) 36–39.
- [8] H.B. Tao, L. Fang, J. Chen, H.B. Yang, J. Gao, J. Miao, S. Chen, B. Liu, *J. Am. Chem. Soc.* 138 (2016) 9978–9985.
- [9] D. Liu, Q. Lu, Y. Luo, X. Sun, A.M. Asiri, *Nanoscale* 7 (2015) 15122–15126.
- [10] K. Jayaramulu, J. Masa, O. Tomanec, D. Peeters, V. Ranc, A. Schneemann, R. Zboril, W. Schuhmann, R.A. Fischer, *Adv. Funct. Mater.* 27 (2017) 1700451.
- [11] H. Wu, B. Xia, L. Yu, X. Yu, X. Lou, *Nat. Commun.* 6 (2015) 6512.
- [12] J. Jiang, Q. Liu, C. Zeng, L. Ai, *J. Mater. Chem. A* 5 (2017) 16929–16935.
- [13] C. Sun, Q. Dong, J. Yang, Z. Dai, J. Lin, P. Chen, W. Huang, X. Dong, *Nano Res.* 9 (2016) 2234–2243.
- [14] C. Panda, P.W. Menezes, C. Walter, S. Yao, M.E. Miehlic, V. Gutkin, K. Meyer, M. Driess, *Angew. Chem. Int. Ed.* 56 (2017) 10506–10510.
- [15] D.V. Shinde, L.D. Trizio, Z. Dang, M. Prato, R. Gaspari, L. Manna, *Chem. Mater.* 29 (2017) 7032–7041.
- [16] W. Chen, K. Sasaki, C. Ma, A.I. Frenkel, N. Marinkovic, J.T. Muckerman, Y. Zhu, R.R. Adzic, *Angew. Chem. Int. Ed.* 51 (2012) 6131–6135.
- [17] J. Huang, Y. Sun, X. Du, Y. Zhang, C. Wu, C. Yan, Y. Yan, G. Zou, W. Wu, R. Lu, Y. Li, J. Xiong, *Adv. Mater.* 30 (2018) 1803367.
- [18] Y. Zhang, X. Xia, X. Cao, B. Zhang, N.H. Tiep, H. He, S. Chen, Y. Huang, H.J. Fan, *Adv. Energy Mater.* 7 (2017) 1700220.
- [19] Y. Pi, Q. Shao, P. Wang, J. Guo, X. Huang, *Adv. Funct. Mater.* 27 (2017) 1700886.
- [20] J. Masa, P. Weide, D. Peeters, I. Sinev, W. Xia, Z. Sun, C. Somsen, M. Muhler, W. Schuhmann, *Adv. Energy Mater.* 6 (2016) 1502313.
- [21] Z. Xue, H. Su, Q. Yu, B. Zhang, H. Wang, X. Li, J. Chen, *Adv. Energy Mater.* 7 (2017) 1602355.
- [22] Z. Zhao, D.E. Schipper, A.P. Leitner, H. Thirumalai, J. Chen, L. Xie, F. Qin, M.K. Alam, L.C. Grabow, S. Chen, D. Wang, Z. Ren, Z. Wang, K.H. Whitmire, J. Bao, *Nano Energy* 39 (2017) 444–453.
- [23] L. Yan, L. Cao, P. Dai, X. Gu, D. Liu, L. Li, Y. Wang, X. Zhao, *Adv. Funct. Mater.* 27 (2017) 1703455.
- [24] J.F. Callejas, J.M. McEnaney, C.G. Read, J.C. Crompton, A.J. Bicchieri, E.J. Popczun, T.R. Gordon, N.S. Lewis, R.E. Schaak, *ACS Nano* 8 (2014) 11101–11107.
- [25] J. Huang, Y. Li, Y. Xia, J. Zhu, Q. Yi, H. Wang, J. Xiong, Y. Sun, G. Zou, *Nano Res.* 10 (2017) 1010–1020.
- [26] S. Wang, L. Zhang, X. Li, C. Li, R. Zhang, Y. Zhang, H. Zhu, *Nano Res.* 10 (2017) 415–425.
- [27] J. Tian, Q. Liu, N. Cheng, A.M. Asiri, X. Sun, *Angew. Chem. Int. Ed.* 53 (2014) 9577–9581.
- [28] J. Yang, F. Zhang, X. Wang, D. He, G. Wu, Q. Yang, X. Hong, Y. Wu, Y. Li, *Angew. Chem. Int. Ed.* 55 (2016) 12854–12858.
- [29] Z. Xing, Q. Liu, A.M. Asiri, X. Sun, *ACS Catal.* 5 (2015) 145–149.
- [30] M.A.R. Anjum, J.S. Lee, *ACS Catal.* 7 (2017) 3030–3038.
- [31] C. Sophie, P. David, B. Cédric, M. Nicolas, S. Clément, *Chem. Rev.* 113 (2013) 7981–8065.
- [32] J. Wu, D. Wang, S. Wan, H. Liu, C. Wang, X. Wang, *Small* (2019) 1900550.
- [33] J. Bao, Z. Wang, J. Xie, L. Xu, F. Lei, M. Guan, Y. Zhao, Y. Huang, H. Li, *Chem. Commun.* 55 (2019) 3521–3524.
- [34] C. Wang, J. Jiang, T. Ding, G. Chen, W. Xu, Q. Yang, *Adv. Mater. Interfaces* 3 (2016) 1500454.
- [35] M.-I. James, X. Sun, *J. Power Sources* 400 (2018) 31–68.
- [36] C. Kuo, Y. Tang, L. Chou, B.T. Sneed, C.N. Brodsky, Z. Zhao, C.F. Tsung, L. Chou, *J. Am. Chem. Soc.* 134 (2012) 14345–14348.
- [37] B.R. Pimentel, A. Parulkar, E.-k. Zhou, N.A. Brunelli, R.P. Lively, *ChemSusChem* 7 (2014) 3202–3240.
- [38] Z. Li, J. Cui, Y. Liu, J. Li, K. Liu, M. Shao, *ACS Appl. Mater. Interfaces* 10 (2018) 34494–34501.
- [39] J. Huang, H. Gao, Y. Xia, Y. Sun, J. Xiong, Y. Li, S. Cong, J. Guo, S. Du, G. Zou, *Nano Energy* 46 (2018) 305–313.
- [40] Y. Wang, Z. Wang, Y. Chen, H. Zhang, M. Yousaf, H. Wu, M. Zou, A. Cao, R.P.S. Han, *Adv. Mater.* 30 (2018) 1802074.
- [41] Z. Fang, L. Peng, Y. Qian, X. Zhang, Y. Xie, J.J. Cha, G. Yu, *J. Am. Chem. Soc.* 140 (2018) 5241–5247.
- [42] B. Xia, Y. Yan, N. Li, H. Wu, X. Lou, X. Wang, *Nat. Energy* 1 (2016) 15006.
- [43] J. Yu, Q. Li, Y. Li, C.-Y. Xu, L. Zhen, V.P. Dravid, J. Wu, *Adv. Funct. Mater.* 26 (2016) 7644–7651.
- [44] J. Huang, Y. Li, Y. Xia, J. Zhu, Q. Yi, H. Wang, J. Xiong, Y. Sun, G. Zou, *Nano Res.* 10 (2017) 1010–1020.
- [45] J. Yin, Q. Fan, Y. Li, F. Cheng, P. Zhou, P. Xi, S. Sun, *J. Am. Chem. Soc.* 138 (2016) 14546–14549.
- [46] C. Du, M. Shang, J. Mao, W. Song, *J. Mater. Chem. A* 5 (2017) 15940–15949.
- [47] F. Niu, Y. Wang, L. Ma, Z. Xie, Y. Wang, C. Wang, Y. Mao, *J. Alloys. Compd.* 778 (2019) 933–941.
- [48] C. Lei, Y. Wang, Y. Hou, P. Liu, J. Yang, T. Zhang, X. Zhuang, M. Chen, B. Yang, L. Lei, C. Yuan, M. Qiu, X. Feng, *Energ. Environ. Sci.* 12 (2019) 149–156.
- [49] P. He, X. Yu, X. Lou, *Angew. Chem. Int. Ed.* 56 (2017) 3897–3900.
- [50] J. Huang, Y. Su, Y. Zhang, W. Wu, C. Wu, Y. Sun, R. Lu, G. Zou, Y. Lia, J. Xiong, *J. Mater. Chem. A* 6 (2018) 9467–9472.
- [51] X. Liang, B. Zheng, L. Chen, J. Zhang, Z. Zhuang, B. Chen, *ACS Appl. Mater. Interfaces* 9 (2017) 23222–23229.
- [52] Y. Tan, H. Wang, P. Liu, Y. Shen, C. Cheng, A. Hirata, T. Fujita, Z. Tang, M. Chen, *Energ. Environ. Sci.* 9 (2016) 2257–2261.
- [53] E.J. Popczun, J.R. McKone, C.G. Read, A.J. Bicchieri, A.M. Wiltrout, N.S. Lewis,

- R.E. Schaak, J. Am. Chem. Soc. 135 (2013) 9267–9270.
- [54] M. Park, J. Ryu, Y. Kima, J. Cho, *Energ. Environ. Sci.* 7 (2014) 3727–3735.
- [55] W. Zhang, X. Yao, S. Zhou, X. Li, L. Li, Z. Yu, L. Gu, *Small* 14 (2018) 1800423.
- [56] H. Chen, K. Shen, Q. Mao, J. Chen, Y. Li, *ACS Catal.* 8 (2018) 1417–1426.
- [57] Y. Pan, K. Sun, S. Liu, X. Cao, K. Wu, W. Cheong, Z. Chen, Y. Wang, Y. Li, Y. Liu, D. Wang, Q. Peng, C. Chen, Y. Li, *J. Am. Chem. Soc.* 140 (2018) 2610–2618.
- [58] J. Yang, X. Wang, B. Li, L. Ma, L. Shi, Y. Xiong, H. Xu, *Adv. Funct. Mater.* 27 (2017) 1606497.
- [59] Z. Zhao, M. Li, L. Zhang, L. Dai, Z. Xia, *Adv. Mater.* 27 (2015) 6834–6840.
- [60] W. Ding, Z. Wei, S. Chen, X. Qi, T. Yang, J. Hu, D. Wang, L. Wan, S.F. Alvi, L. Li, *Angew. Chem.* 125 (2013) 11971–11975.
- [61] D. Guo, R. Shibuya, C. Akiba, S. Saji, T. Kondo, J. Nakamura, *Science* 351 (2016) 361–365.
- [62] H. Jin, J. Wang, D. Su, Z. Wei, Z. Pang, Y. Wang, *J. Am. Chem. Soc.* 137 (2015) 2688–2694.
- [63] C. Sophie, P. David, B. Cédric, M. Nicolas, S. Clément, *Chem. Rev.* 113 (2013) 7981–8065.
- [64] X. Dai, K. Du, Z. Li, M. Liu, Y. Ma, H. Sun, X. Zhang, Y. Yang, *ACS Appl. Mater. Interfaces* 7 (2015) 27242–27253.
- [65] J. Xie, H. Zhang, S. Li, R. Wang, X. Sun, M. Zhou, J. Zhou, X. Lou, Y. Xie, *Adv. Mater.* 25 (2013) 5807–5813.
- [66] B. Konkena, J. Masa, A.J.R. Botz, I. Sinev, W. Xia, J. Kossmann, R. Drautz, M. Muhler, W. Schuhmann, *ACS Catal.* 7 (2017) 229–237.
- [67] K. Liu, F. Wang, P. He, T.A. Shifa, Z. Wang, Z. Cheng, X. Zhan, J. He, *Adv. Energy Mater.* 8 (2018) 1703290.